


Thermodynamics of underdamped Brownian collisional engines: General features and resonant phenomena

Gustavo A. L. Forão¹,[✉] Fernando S. Filho^{1,2},[✉] Bruno A. N. Akasaki¹,[✉] and Carlos E. Fiore¹,[✉]

¹*Universidade de São Paulo, Instituto de Física, Rua do Matão, 1371, 05508-090 São Paulo, SP, Brazil*

²*UHasselt, Faculty of Sciences, Theory Lab, Agoralaan, 3590 Diepenbeek, Belgium*

 (Received 5 July 2024; revised 17 September 2024; accepted 11 October 2024; published 20 November 2024)

Collisional Brownian engines have been proposed as alternatives to nonequilibrium nanoscale engines. However, most studies have focused on the simpler overdamped case, leaving the role of inertia much less explored. In this work, we introduce the idea of collisional engines to underdamped Brownian particles, where at each stage the particle is sequentially subjected to a distinct driving force. A careful comparison between the performance of underdamped and overdamped Brownian work-to-work engines has been undertaken. The results show that underdamped Brownian engines generally outperform their overdamped counterparts. A key difference is the presence of a resonant regime in underdamped engines, in which both efficiency and power output are enhanced across a broad set of parameters. Our study highlights the importance of carefully selecting dynamics and driving protocols to achieve optimal engine performance.

DOI: [10.1103/PhysRevE.110.054125](https://doi.org/10.1103/PhysRevE.110.054125)

I. INTRODUCTION

The performance of engines and the search for protocol optimizations constitute fundamental issues in thermodynamics since the seminal work by Carnot [1,2] in 1872. Notwithstanding, the construction of different and reliable engine setups aimed at converting one kind of energy into another one has become more sophisticated, above all with the advent of nanotechnology and new experimental procedures for investigating and creating nanoscale engines. Contrasting with macroscopic engines, fluctuations in nanoscale systems can become important, making necessary the use of stochastic methods in order to describe their dynamics and thermodynamic properties, as well as its relationship with the system performance. Stochastic thermodynamics (ST) constitutes a unified tool for describing nanoscale systems operating far from equilibrium [3–6] and addressing the role of fluctuations and dissipation.

Recently, a collisional (or sequential) description has been proposed and extended for Brownian systems [7–10]. In its simplest version, a single particle interacts sequentially with a thermal bath and is subjected to a specific work source at each stage. This approach differs from the situation where the system interacts with all thermal baths simultaneously [11,12] and has been studied in distinct cases of nonequilibrium thermodynamics [13,14], open quantum systems [14–17], and information and computational processing [14,18–20]. Under suitable conditions, the sequential interaction operates as a heat engine or work-to-work converters, generating useful power. Despite this, its performance can be small or strongly reduced depending on the way it is designed, suggesting the choice of ingredients such as period, the duration of each stage, temperatures, the strength of driving worksources, and others as fundamental [7–9,13,21].

For describing the motion of particles in a colloidal environment subjected to random forces, a fundamental framework is the Langevin equation or Fokker-Planck approach [22,23]. Its two employed variants, namely the underdamped and overdamped cases, capture distinct and essential aspects of particle dynamics and stochasticity. The underdamped variant emphasizes inertia and retains the correlation between particle and position, while the overdamped variant simplifies the description and is suitable for systems with rapid relaxation. Despite the extensive research about them [24–31], little is known about their thermodynamic implications and the influence of inertial considerations on system performance and dissipation [11,12].

In this paper, we advance upon previous works [7–10] by introducing and extending the concept of collisional Brownian engines to underdamped systems. For equal temperatures at each stage, we obtain exact expressions for Thermodynamic quantities such as work, heat, and dissipation, solely expressed in terms of Onsager coefficients, irrespective of the driving protocol. For distinct driving worksources, we provide a comparative study between underdamped and overdamped dynamics. The underdamped case is significantly different [7–10] due to the presence of a resonance phenomenon, resulting in a specific region on the phase space in which the engine operates at maximum power and maximum efficiency. The present study sheds light on the importance of dynamics and driving protocols for achieving optimal engine performances.

This paper is structured as follows: In Sec. I, we introduce the model, present the main expressions for the underdamped system, and discuss the optimization approaches. In Sec. II, we compare the performance and dissipation of engines governed by each dynamic and highlight the resonant phenomena in the underdamped engine. Finally, conclusions are drawn in Sec. III.

II. THERMODYNAMICS OF UNDERDAMPED BROWNIAN ENGINES

Our setup is composed of a Brownian particle sequentially placed in contact with a given thermal reservoir and subjected to a total force $\bar{f}_i(x, t)$ per mass at each stage i , $i \in \{1, 2\}$. The former and latter contact has duration τ_1 and $\tau - \tau_1$, respectively, in which at each stroke i , the system dynamics is described by the equations,

$$\begin{aligned} \frac{d}{dt} v_i(t) &= \bar{f}_i(x, t) - \gamma_i v_i(t) + \xi_i(t), \\ \frac{d}{dt} x_i(t) &= v_i(t). \end{aligned} \quad (1)$$

Here, γ_i represents the viscous coefficient per mass. The stochastic forces follow standard white noise properties: $\langle \xi_i(t) \rangle = 0$ and $\langle \xi_i(t) \xi_j(t') \rangle = 2\gamma_i k_B T_i \delta_{ij} \delta(t - t')/m$. The probability distribution of the particle $P_i(x, v, t)$ at the stroke i is described by Fokker-Planck-Kramers (FPK) [5,7,23,32],

$$\frac{\partial P_i}{\partial t} = - \left[v \frac{\partial P_i}{\partial x} + \bar{f}_i(x, t) \frac{\partial P_i}{\partial v} + \frac{\partial J_i}{\partial v} \right], \quad (2)$$

where $\bar{f}_i(x, t)$ is decomposed in the following form $\bar{f}_i(x, t) = f_i^*(x) + \tilde{f}_i(t)$, where $f_i^*(x) = -\kappa x_i/m$ depends on the position, $\tilde{f}_i(t)$ is time dependent and J_i is a current of probability given by

$$J_i = -\gamma_i v P_i - \frac{\gamma_i k_B T_i}{m} \frac{\partial P_i}{\partial v}. \quad (3)$$

At $t = \tau_1$, the particle switches to a second thermal bath at temperature T_2 and is subjected to a second force $\tilde{f}_2(x, t)$, which acts during the interval $t \in [\tau_1, \tau)$. At $t = \tau$, a cycle is completed, and the particle returns to the first thermal bath with T_1 and $\tilde{f}_1(x, t)$, starting a new cycle. The collisional approach assumes the exchange of reservoirs happens instantaneously, effectively treating each switching as an adiabatic process. Some remarks about Eq. (2) are in order. First, the probability distribution has Gaussian form regardless of the temperatures and drivings. Second, the specific case where $\tilde{f}_1(t) = \tilde{f}_2(t) = 0$ and the temperatures are equal, $T_1 = T_2$, corresponds to the Boltzmann-Gibbs distribution, describing equilibrium thermodynamics. Third, even when $T_1 \neq T_2$ and/or $\tilde{f}_1(t) \neq \tilde{f}_2(t)$, the system evolves towards a nonequilibrium steady state (NESS). Lastly, in deriving the model's thermodynamics, we assume that both $P_i(v, x, t)$ and $J_i(v, x, t)$ vanish as $v \rightarrow \pm\infty$ and/or $x \rightarrow \pm\infty$. The mean energy $U_i(t) = m\langle v_i^2 \rangle/2 + \kappa\langle x_i^2 \rangle/2$ has the time derivative expressed as the sum of two components,

$$\frac{d}{dt} U_i(t) = -[\dot{W}_i(t) + \dot{Q}_i(t)], \quad (4)$$

where the former and latter right terms denote the work (per time) done on the particle by the force $\tilde{f}_i(t)$ and the heat flux $\dot{Q}_i(t)$ exchanged with the thermal bath at the stroke i . Explicitly,

$$\dot{W}_i(t) = -m \langle v_i \rangle(t) \tilde{f}_i(t) \quad (5)$$

and

$$\dot{Q}_i(t) = \gamma_i (m \langle v_i^2 \rangle(t) - k_B T_i), \quad (6)$$

respectively. From now on, we shall restrict ourselves to the case where $\tau_1 = \tau/2$, in which the external drivings can be expressed in the following form:

$$\tilde{f}_i(t) = \begin{cases} X_1 g_1(t), & 0 \leq t < \tau/2 \\ X_2 g_2(t), & \tau/2 \leq t < \tau, \end{cases} \quad (7)$$

where the X_i denotes the strength of the thermodynamic force per mass acting on the system, whereas $g_i(t)$ defines the shape of the protocol. By evaluating (4) over a complete cycle and considering that the system returns to its initial state, one derives the first law of thermodynamics averaged over a period in NESS: $\bar{W}_1 + \bar{W}_2 + \bar{Q}_1 + \bar{Q}_2 = 0$. Similarly, the second law of thermodynamics relates to the time evolution of entropy $S_i = -k_B \langle \ln P_i \rangle$, which, together with Eq. (2), can be expressed through the difference between the entropy production rate $\sigma_i(t)$ and the entropy flux $\Phi_i(t)$:

$$\frac{d}{dt} S_i = \sigma_i(t) - \Phi_i(t), \quad (8)$$

where

$$\sigma_i(t) = \frac{m}{\gamma_i T_i} \int \frac{J_i^2}{P_i} dx dv \quad \text{and} \quad \Phi_i(t) = \frac{\dot{Q}_i(t)}{T_i}. \quad (9)$$

It is straightforward that $\sigma_i(t) \geq 0$, in accordance with the second law of thermodynamics. By evaluating the entropy S_i over the complete period, one has that $\bar{\sigma} = \bar{\Phi} = -(\bar{Q}_1/T_1 + \bar{Q}_2/T_2)$, where $\bar{\sigma} = (\int_0^{\tau_1} \sigma_1(t) dt + \int_{\tau_1}^{\tau} \sigma_2(t) dt)/\tau$ and $\bar{\Phi} = (\int_0^{\tau_1} \Phi_1(t) dt + \int_{\tau_1}^{\tau} \Phi_2(t) dt)/\tau$. We can also relate $\bar{\sigma}$ with components \bar{Q}_i 's and \bar{W}_i 's by means of the following expression:

$$\bar{\sigma} = \frac{4T^2}{4T^2 - \Delta T^2} \left[\frac{-(\bar{W}_1 + \bar{W}_2)}{T} + \frac{(\bar{Q}_1 - \bar{Q}_2) \Delta T}{2T^2} \right], \quad (10)$$

where we introduce the variables $T = (T_1 + T_2)/2$ and $\Delta T = T_1 - T_2$, together the first law of thermodynamics. Since one of our goals is to compare overdamped and underdamped setups, we will focus on the simplest case where the temperatures are equal ($\Delta T = 0$), resulting in the system having only two thermodynamic forces, closely related to X_1 and X_2 . By adjusting X_1 and X_2 , the system can operate as a work-to-work converter, generating useful power output during one of the two strokes. Numerous examples exist in Brownian engines and biological physics where work-to-work converters operate [3,26,27,33–36], converting energy (e.g., chemical or mechanical) into power output.

In this case, Eq. (10) reduces to

$$\bar{\sigma} = \frac{-(\bar{W}_1 + \bar{W}_2)}{T}. \quad (11)$$

In order to exploit the driving changes at each stroke, we express $g_i(t)$ in terms of its Fourier components. More specifically,

$$g_1(t) = \frac{a_0}{2} + \sum_{n=1}^{\infty} a_n \cos\left(\frac{2\pi n t}{\tau}\right) + b_n \sin\left(\frac{2\pi n t}{\tau}\right) \quad (12)$$

and

$$g_2(t) = \frac{c_0}{2} + \sum_{n=1}^{\infty} c_n \cos\left(\frac{2\pi n t}{\tau}\right) + d_n \sin\left(\frac{2\pi n t}{\tau}\right), \quad (13)$$

respectively, where the driving to be considered is characterized by obtaining the coefficients a_n , b_n , c_n , and d_n under the conditions $c_n = d_n = 0$ for $i = 1$ and $a_n = b_n = 0$ for $i = 2$. It is worth mentioning that Fourier representation ensures the boundary conditions with respect to the probability continuity at $t = \tau/2$ and the fact the system returns to the initial state at $t = \tau$. By averaging Eq. (1), one finds the following general expression for $\langle v \rangle(t)$:

$$\begin{aligned} \langle v \rangle(t) = & \sum_{k=1}^{\infty} (X_1 \cdot a_{1vk} + X_2 \cdot a_{2vk}) \cos\left(\frac{2\pi k t}{\tau}\right) \\ & + (X_1 \cdot b_{1vk} + X_2 \cdot b_{2vk}) \sin\left(\frac{2\pi k t}{\tau}\right), \end{aligned} \quad (14)$$

where a_{ivk} and b_{ivk} correspond to Fourier coefficients obtained for the mean velocity and depend on the driving form from Eqs. (12) and (13). Its explicit form is shown in Appendix B. By plugging Eq. (14) into Eq. (5) and averaging over the duration of each stroke, \bar{W}_1 and \bar{W}_2 can be expressed in terms of fluxes J_i 's and thermodynamic forces $f_i = X_i/T$ ($i \in \{1, 2\}$) given by

$$\bar{W}_1 = -T J_1 f_1 = -T (L_{11} f_1^2 + L_{12} f_1 f_2), \quad (15)$$

$$\bar{W}_2 = -T J_2 f_2 = -T (L_{22} f_2^2 + L_{21} f_2 f_1), \quad (16)$$

where L_{ij} denote the Onsager coefficients, with their main expressions listed in Appendix B. In the regime of small ΔT , Eq. (10) can be rewritten as $\bar{\sigma} \approx J_1 f_1 + J_2 f_2 + J_T f_T$, where the thermodynamic flux J_T is given by $J_T = L_{TT} f_T$. Here, $f_T = \Delta T/T^2$, and L_{TT} represents the corresponding Onsager coefficient. Since we are focused on the isothermal case, $f_T = 0$. Moreover, similar to the overdamped case, there is no coupling between work fluxes and heat flux, implying that $L_{1T} = L_{T1} = L_{2T} = L_{T2} = 0$, consistent with the fact that this class of engines operates solely as work-to-work converters, rather than converting heat into work output.

In order for the system to operate as a work-to-work converter, it is required an amount of $\bar{W}_{in} = \bar{W}_i$ be partially converted into work output $\mathcal{P} = \bar{W}_{out} = \bar{W}_j$, where $\mathcal{P} \geq 0 > \bar{W}_{in}$ and $|\bar{W}_{in}| > \mathcal{P}$. The efficiency of such conversion is thus given by

$$\eta \equiv -\frac{\mathcal{P}}{\bar{W}_{in}}, \quad (17)$$

where $0 \leq \eta \leq 1$. Notice that, for certain parameter ranges, \bar{W}_j can exceed \bar{W}_i , meaning that in such cases, the input work $\bar{W}_{in} = \bar{W}_j$ is partially converted into output work $\bar{W}_{out} = \bar{W}_i$. Hence, when $\tilde{f}_i \leftrightarrow \tilde{f}_j$, it follows that $\bar{W}_{in} \leftrightarrow \bar{W}_{out}$, implying $\eta \leftrightarrow 1/\eta$. This regime change is further discussed in Appendix C. When expressed in terms of Onsager coefficients and thermodynamic forces, η is given by

$$\eta = -\frac{J_j f_j}{J_i f_i} = -\frac{L_{jj} f_j^2 + L_{ji} f_i f_j}{L_{ii} f_i^2 + L_{ij} f_j f_i}. \quad (18)$$

Overview about system maximizations

There are distinct routes for optimizing power and efficiency in Brownian work-to-work converters. As stated in previous works [8,9,11], it is possible to express their optimized values in terms of Onsager coefficients. In this section, we briefly review these methods.

Starting with the power and considering that f_i is held fixed, the engine regime is constrained by $0 < f_j < |f_m|$, where $f_m = -L_{ji} f_i / L_{jj}$. The force f_j^{MP} that ensures maximum power \mathcal{P}_{MP} is given by $f_j^{\text{MP}} = -L_{ji} f_i / 2L_{jj} = f_m/2$. By inserting this relation into Eqs. (16) and (18), we obtain the following expressions for quantities at maximum power:

$$\mathcal{P}_{\text{MP}} = T \frac{L_{ji}^2}{4 L_{jj}} f_i^2, \quad \eta_{\text{MP}} = \frac{L_{ji}^2}{4 L_{jj} L_{ii} - 2 L_{ji} L_{ij}}. \quad (19)$$

Alternatively, one can search for f_j^{ME} by optimizing the efficiency with respect to f_j ,

$$f_j^{\text{ME}} = \frac{L_{ii}}{L_{ij}} \left(-1 + \sqrt{1 - \frac{L_{ji} L_{ij}}{L_{jj} L_{ii}}} \right) f_i, \quad (20)$$

and associated maximum efficiency is given by

$$\eta_{\text{ME}} = -\frac{L_{ji}}{L_{ij}} + \frac{2 L_{ii} L_{jj}}{L_{ij}^2} \left(1 - \sqrt{1 - \frac{L_{ij} L_{ji}}{L_{ii} L_{jj}}} \right), \quad (21)$$

and corresponding \mathcal{P}_{ME} is obtained by inserting f_j^{ME} into the expression for \mathcal{P} , respectively.

We close this section by pointing out the role of distinct temperatures. First, both \bar{W}_1 and \bar{W}_2 are independent on temperatures for the sort of drivings we shall consider and, hence, \mathcal{P} remains unchanged. On the other hand, η will not be affected and $\bar{\sigma}$ is modified only by a rescaling of temperatures for work-to-work converters. However, the situation changes when temperatures vary at each stroke, since \bar{Q}_1 and \bar{Q}_2 will differ due to the inclusion of a term proportional to the temperature difference. Since both \bar{W}_1 and \bar{W}_2 remain unchanged, η is expected to decrease in general.

III. RESULTS

Unless explicitly stated otherwise, we shall adopt $k_B = m = 1$, $\gamma_1 = \gamma_2 = \gamma$ and analysis will be carried out for distinct τ 's, f_j 's, and κ 's. In order to draw a comparison with previous results (see, e.g., Refs. [7–10]), we have opted for depicting the main results in without units. In this section, we draw a comparison between underdamped and overdamped Brownian engines for different driving forces. Our analysis assumes a constant (square wave) driving, given by $g_1(t) = g_2(t) = 1$, and a linear (sawtooth) driving, given by

$$g_i(t) = \begin{cases} \lambda t, & 0 < t \leq \tau/2 \\ \lambda(t - \tau/2), & \tau/2 < t \leq \tau, \end{cases} \quad (22)$$

where λ is a constant introduced in such a way $g_i(t)$ is dimensionless. In all cases we set $\lambda = 1$. Fourier components of each driving protocol can be found in Appendix B. For completeness, we also investigate sinusoidal drivings at each stage, as can be seen in Appendix D.

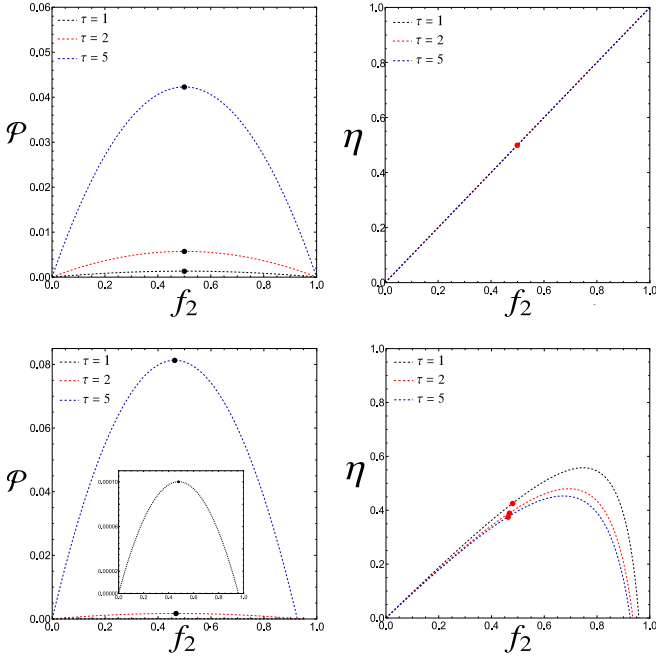


FIG. 1. For the underdamped case, the depiction of the power output \mathcal{P} (left) and efficiency η (right) as functions of f_2 for constant (top) and linear (bottom) drivings and different periods τ . Black and red dots represent \mathcal{P}_{MP} and η_{MP} , respectively. Parameters: $f_1 = T = 1$, $\gamma = 1$, and $\kappa = 1$.

A. Dynamics comparison: Performance contrast

In order to obtain a first insight into the similarities and differences between underdamped and overdamped collisional Brownian engines, Figs. 1 and 2 depict, for distinct periods τ 's, the power and efficiency versus the force $X_2 = T f_2$ for constant and linear drivings for the underdamped and overdamped regimes, respectively. To simplify matters, this first analysis will be carried out for $\gamma = \kappa = 1$. In both cases, the system can operate as a work-to-work converter by choosing f_2 constrained between 0 and $|f_m|$. We point out some remarkable differences between them, which can be understood from the relationship among quantities and Onsager coefficients. For the (underdamped) constant protocol, expressions for Onsager coefficients (listed in Appendix B) obey a special symmetry $L_{11} = L_{22} = -L_{12} = -L_{21}$. As a consequence, the engine regime is delimited by $0 \leq f_2 \leq f_m = f_1$ (for all values of τ), and both \mathcal{P} and η acquire simple forms, given by $\mathcal{P} = L_{22}f_2(f_2 - f_1)$ and $\eta = f_2/f_1$, respectively. As a result η solely depends on the ratio between forces, followed by maximum efficiency and maximum power occurring at $f_2^{ME} = f_1$ and $f_2^{MP} = f_1/2$, respectively, irrespective the values of κ , ω , and τ . Maximum values are promptly obtained from Eqs. (19)–(21) and read $\eta_{MP} = 1/2$, $\eta_{ME} = 1$, $\mathcal{P}_{MP} = TL_{22}f_1^2/4$. While the former two are independent on the period, there is an optimal period τ_o providing maximum \mathcal{P}_{MP} because L'_{ij} s exhibit a nonmonotonic behavior as τ increases. In particular, for the sort of parameters \mathcal{P}_{MP} is peaked at, $\tau_o = 6.311\dots$, with a maximum given by $\mathcal{P}_{MP} = 0.05148$ for $f_1 = 1$. All such features are quite different from the overdamped case where the engine regime is strongly dependent on τ . In particular, both power and efficiencies decrease as τ

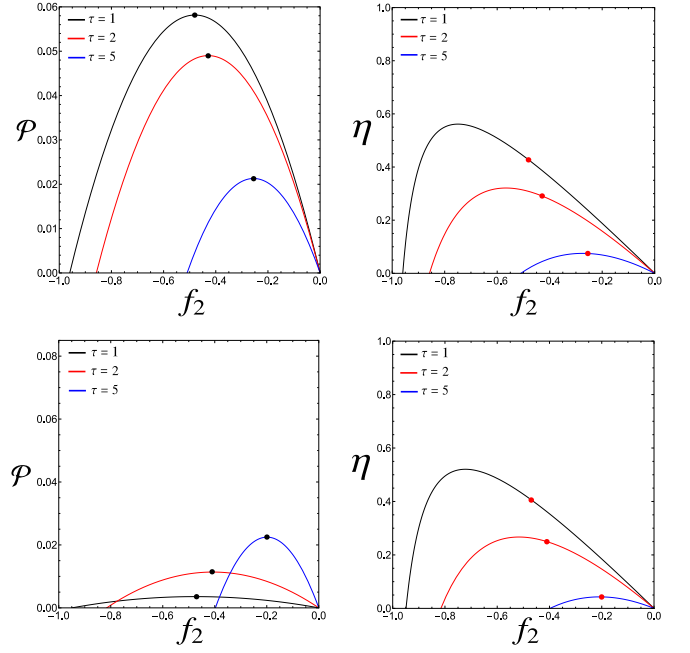


FIG. 2. For the overdamped case, the depiction of the power output \mathcal{P} (left) and efficiency η (right) as functions of f_2 for constant (top) and linear (bottom) drivings and different periods τ . Again, black and red dots represent \mathcal{P}_{MP} and η_{MP} , respectively. Parameters: $f_1 = T = 1$ and $\gamma = 1$.

is increased (see, e.g., left panels). Conversely, \mathcal{P}_{MP} decreases as τ is increased for the overdamped case.

The linear case is more revealing. Although Onsager coefficients also satisfy the relations $L_{11} = L_{22}$ and $L_{12} = L_{21}$, one has $L_{11} \neq -L_{12}$, and the ratio L_{11}/L_{22} increases “faster” than L_{12}/L_{21} as τ is increased. As a first consequence, f_m behaves differently from the constant case and smoothly decreases as τ is increased. Also, optimized quantities \mathcal{P}_{MP} , η_{MP} , \mathcal{P}_{ME} , and η_{ME} behave differently from the constant case and depend on the interplay between κ and τ . For $\kappa = f_1 = 1$, \mathcal{P}_{MP} is maximum for $\tau_o = 7.345\dots$, whose associate power and efficiency are given by $\mathcal{P}_{MP} = 0.170\dots$ and $\eta_{MP} = 0.2765\dots$, respectively. The overdamped case also presents an optimal τ_o ensuring maximum \mathcal{P}_{MP} . In particular, for $f_1 = \gamma = 1$, it occurs at $\tau_o = 4.695\dots$ with a substantially lower maximum power $\mathcal{P}_{MP} = 0.0224\dots$

The differences between underdamped and overdamped cases can be understood in terms of some heuristic (non rigorous) arguments. We first note that, for a given protocol, strength driving forces in overdamped and underdamped cases operate in opposite and same directions in the work-to-work regime, respectively. This is because there is no need for an extra force to bring the system back to its initial position in the latter case, while in the former (overdamped) case, due to the absence of a restoring potential, it is essential for the system to have both drivings acting in different directions in order to generate useful power. Such findings seem to be general and have also been verified for periodic protocols. However, there are some subtleties for sinusoidal drivings, partly due to the phase difference between drivings (see Appendix D). Another difference between underdamped and overdamped lies in the interplay between f_m and τ . Although it can be

understood directly from Onsager coefficients, our heuristic argument suggests that the mean velocity aligns with the external force in both stages (for the overdamped case) for sufficiently long periods and hence no useful power output is generated. This is quite different from the underdamped case, where the influence of the restoring force and its interplay with period and driving lead to different behaviors.

B. Deterministic resonant phenomena in underdamped dynamics

The presence of a restoring potential in the underdamped case results in a resonant phenomena when an external force drives on the system and can significantly influence its performance and the behavior of thermodynamic quantities. Such phenomena shares some similarities with the so-called stochastic resonance (SR), recently verified in an experimental study involving interacting resonant Brownian [37]. In the present case, our goal is to study the effects of deterministic resonance due to external driving at each stroke.

We start this section by deriving the resonant κ_{res} in terms of the system's parameters. The external driving is also a periodic force with total period τ and frequency $\omega = 2\pi/\tau$. The k th contribution to the Fourier series of the mean velocity (14) is expressed as

$$\begin{aligned} \langle v(t) \rangle^{k\text{-th}} = & (X_1 \cdot a_{1vk} + X_2 \cdot a_{2vk}) \cos\left(\frac{2\pi k t}{\tau}\right) \\ & + (X_1 \cdot b_{1vk} + X_2 \cdot b_{2vk}) \sin\left(\frac{2\pi k t}{\tau}\right). \end{aligned} \quad (23)$$

The resonant phenomena is characterized by a maximum of amplitude of $\langle v(t) \rangle^{k\text{-th}}$ with respect to the time t and κ , described by the following relation:

$$\kappa_{\text{res}} = \left(\frac{2\pi k}{\tau}\right)^2, \quad k \text{ integer}. \quad (24)$$

Such a result is protocol independent, solely depending on the natural frequency $\omega_0 = 2\pi/\tau$, and hence valid for any generic external driving. The relationship between resonance and system performance is depicted in Fig. 3 for constant and linear drivings. We first note that it can remarkably influence the system performance, not only as forces f_1/f_2 are varied (not shown), but also for their optimized values $\mathcal{P}_{MP}/\eta_{MP}$ and $\mathcal{P}_{ME}/\eta_{ME}$ evaluated at $f_2 = f_2^{\text{MP}}$ and $f_2 = f_2^{\text{ME}}$, respectively. In both cases, resonance lines (continuous lines in heat maps) obey Eq. (24) and are followed by increases of power and efficiency for constant and linear drivings for odd and any integer k , respectively. A direct inspection of Eq. (24) for constant drivings reveals that $\langle v(t) \rangle^{k\text{-th}} \ll 1$ for even k , leading to very small performances in such cases. The bottom left panels reinforce these findings for $\kappa = 4\pi^2$ in which $\tau_{\text{res}} = k$. Also, in accordance with what was stated in the previous section, η_{MP} and η_{ME} are always constant in such a case for constant protocols. As a complementary analysis, we also compare numerically the performances at the resonance and out of the resonance. For example, for $\tau = 5$, $\kappa_{\text{res}} = 4\pi^2/25$, and $\kappa = 1$, both constant (linear) drivings show that the system operates with higher performances at resonance $\mathcal{P}_{MP} = 5, 12 \cdot 10^{-2}$ (9, 91 $\cdot 10^{-2}$) than out of resonance

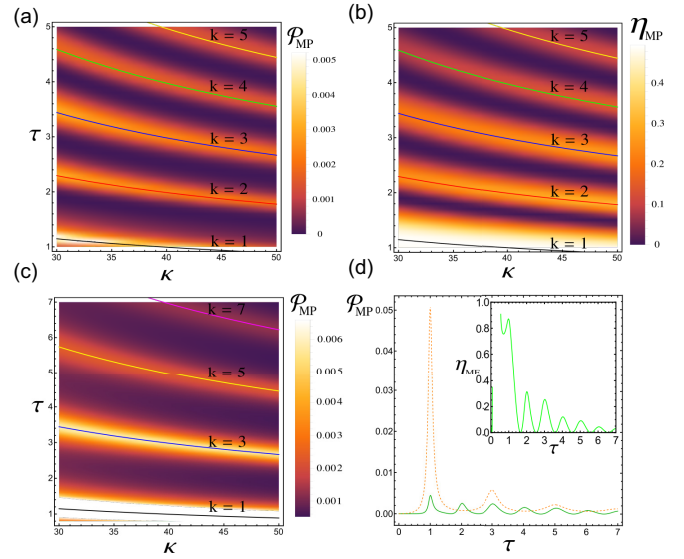


FIG. 3. Top panels: (a) depicts the maximum power \mathcal{P}_{MP} and (b) depicts the efficiency at maximum power η_{MP} heat maps for linear drivings. (c) shows the same, but for constant drivings. Continuous lines show the resonance lines according to Eq. (24). All maximizations have been carried out with respect to f_2 . Since $\eta_{MP} = 1/2$ for constant drivings, heat maps in such a case have not been shown. In (d), there is a plot of \mathcal{P}_{MP} for constant (dashed) and linear (continuous) drivings for $\kappa = 4\pi^2$. Inset: the same but for η_{ME} (linear). Parameters: $f_1 = T = 1$ and $\gamma = 1$.

$\mathcal{P}_{MP} = 4, 23 \cdot 10^{-2}$ (8, 12 $\cdot 10^{-2}$), respectively, but in both cases, efficiencies are close to each other, with $\eta_{MP} = 1/2$ (0.38). Hence, the existence of resonance in the underdamped case can provide a remarkable advantage over the overdamped dynamics, not only because it is protocol independent but also because it can enhance power without sacrificing efficiency. However, a common trait of all resonance patterns is that they are associated with increasing dissipation (see, e.g., right panels in Fig. 5). Similar findings are also observed for harmonic drivings, as depicted in Appendix D for drivings dephased of π at each stroke. As a consequence, resonance lines, maximum \mathcal{P}_{MP} and η_{ME} are also half period translated (see, e.g., Fig. 8). As a final comment, although resonance points are very close to the peaks of \mathcal{P}_{MP} and η_{ME} (inset), they do not precisely coincide (although differences typically yield at the third decimal level).

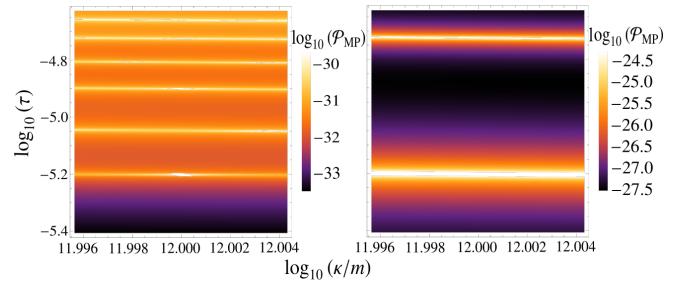


FIG. 4. The power output for the linear (left) and constant (right) protocols in log base ten scale considering some experimental quantities. Here, we use $m \approx 10^{-18}$ kg and $\gamma \approx 10^{-20}$ s $^{-1}$.

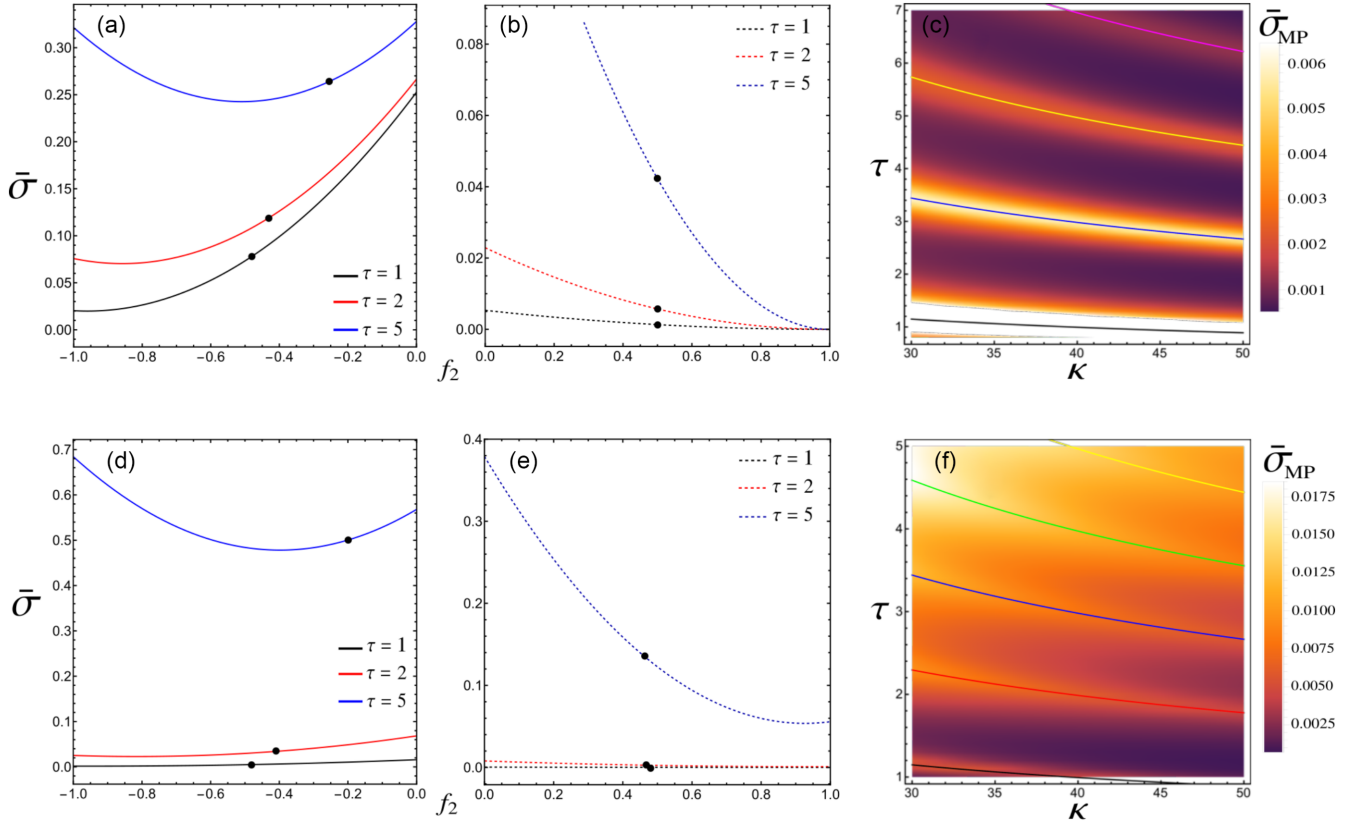


FIG. 5. Left and center panels depict the mean entropy production $\bar{\sigma}$ for the overdamped [(a) and (d)] and underdamped [(b) and (e)] versus f_2 for the same range, resonant lines, and parameters as in Fig. (7). Black dots represent attempts to the maximum power. Panels (c) and (f) show entropy production heat maps for the same parameters from Fig. (3). Top and bottom panels attempt to the constant and linear drivings, respectively. Parameters: $f_1 = 1$, $\gamma = 1$, and $T = 1$ in all plots and $\kappa = 1$ for the 2D plots.

We close this section by estimating how resonant phenomena can be feasible from an experimental point of view. In principle, our framework could be tested using optical tweezer systems, in which the harmonic potential and the external drives can be generated via controlled electric fields [38–41]. For that, we take some values for laboratory quantities: $m \approx 10^{-18}$ kg, $\gamma \approx 10^{-20} \text{s}^{-1}$ by imposing the thermodynamics force $X_1 \approx 0.003$ fN/kg in the underdamped case ($m/\gamma \gg 1$), and in room temperature with $\kappa \approx 1$ $\mu\text{N/m}$. For such values, the resonant regime peaks at $X_2 \approx 0.5$ fN/kg with a period $\tau \approx 6$ μs in the constant case. Figure 4 depicts the maximum power heat maps (J/s) for constant and linear protocols for parameters described above. As in Fig. 3, resonance positions coincide in both constant and linear drivings, consistent to be protocol independent. Also in accordance to previous results, linear drivings present more resonance lines. Although heat maps suggest that resonances can be experimentally verified, it requires a fine tuning of model parameters, indicating that a small perturbation of parameters (e.g., the time cycle and/or in the harmonic potential) can shift the particle from the resonance region.

C. Entropy production

Dynamics comparison and dissipation at resonant regimes

The entropy production has been recognized as a key indicator of system dissipation, being investigated in

distinct contexts, such as in the existence of different trade-offs between dissipation and fluctuation, expressed via TURs [42–45], its interplay or compromise with power and efficiency in the context of thermal engines [7–9,46,47], or even its usage for the characterization of phase transition regimes [48–50]. Despite the fact that it is commonly desired to minimize entropy production and simultaneously maximize power and/or efficiency, the second law of thermodynamics precludes all of these goals from being simultaneously satisfied. With this in mind, this section aims to depict the entropy production behavior of our collisional (underdamped Brownian) engine regimes, above all at the resonance regimes, as well as drawing a comparison with overdamped dynamics. In terms of Onsager coefficients, Eq. (11) acquires the form $\bar{\sigma} = L_{11}f_1^2 + L_{22}f_2^2 + (L_{12} + L_{21})f_1f_2$. In order to obtain insight, Fig. 9 depicts, for the same parameters as in Figs. 1–3, the behavior of entropy production $\bar{\sigma}$ versus f_2 and $\bar{\sigma}_{MP}$ heat maps, evaluated at $f_2 = f_2^{MP}$, respectively. Starting with constant protocol, it takes a simple form $\bar{\sigma} = L_{22}(f_2 - f_1)^2$, meaning that its minimum value $\bar{\sigma}_{mS} = 0$ coincides with the maximum efficiency point $f_2^{ME} = f_1$, irrespective of the period and model parameters. This differs from the overdamped case, not only because $\bar{\sigma}_{mS}$ increases as τ is increased (overdamped) but also the underdamped case is characterized by $0 = \bar{\sigma}_{mS} \neq \bar{\sigma}_m > 0$ (for the overdamped case one has $\bar{\sigma}_m = \bar{\sigma}_{mS} > 0$). Another important comparison involves the behavior of $\bar{\sigma}_{MP}$ and $\bar{\sigma}_{ME}$ (not shown). Both of them increase as τ is increased. However

the underdamped case permits κ to be adjusted to control the dissipation rather than the overdamped case, or even to ensure the desirable compromise between power, efficiency, and dissipation (e.g., for the parameters in Fig. 5, τ and κ can be adjusted for ensuring larger \mathcal{P} 's and lower $\bar{\sigma}$'s).

Lastly, we address the consequences for the dissipation in the resonant regime, as depicted by the right panels of Fig. 5 for the same parameters as in Fig. 3. Resonance patterns are also manifested in the entropy production behavior. Apart from the explanation in terms of Onsager coefficients, we present an alternative argument for the constant protocol. Since $\eta_{MP} = 1/2$ implies that $\bar{W}_1 = -2\bar{W}_2$, the entropy production acquires the simple form $\bar{\sigma}_{MP} = \bar{W}_2/T$, meaning that dissipation heat maps behave similarly to the power heat map, albeit by a factor T . Although the above similar relation is not presented for the linear protocol, resonant patterns are still visible, but less pronounced than power output and efficiency heat maps. This is because entropy production in such cases assumes values close to those outside the resonance lines.

IV. CONCLUSIONS

In this paper, we introduced a sequential engine description for underdamped Brownian engines in which the particle is subjected to distinct worksources at each stage. Exact thermodynamic quantities were obtained from the framework of stochastic thermodynamics. The influence of distinct driving protocols and a detailed comparison with its overdamped dynamics were undertaken. Our findings highlighted the remarkable advantages of the underdamped dynamics when compared with its overdamped counterpart, particularly in scenarios where minimizing dissipation while maximizing power is crucial. Despite the overdamped dynamics exhibiting superior performance in some specific cases, it is typically more dissipative, less efficient, and presents inferior power outputs. Furthermore, the second main feature of the underdamped case is the existence of resonance lines, which can significantly enhance the system's performance. The resonance regime not only increases the power but also enables such enhancements without compromising efficiency. This underscores the role of such phenomena as a mechanism for optimizing engine operation and opens possibilities for the development of efficient and versatile Brownian engines. Overall, our comparative analysis emphasizes the importance of carefully selecting dynamics and driving protocols to optimize engine performance.

ACKNOWLEDGMENT

The authors acknowledge financial support from CNPq and FAPESP under Grants No. 2021/03372-2, No. 2022/16192-5, No. 2022/15453-0, and No. 2024/03763-0.

APPENDIX A: GENERAL FEATURES ABOUT OVERDAMPED BROWNIAN ENGINES

Here we briefly describe the main features of the overdamped version, in conformity with Refs. [7–10]. Consider a Brownian particle of mass m in contact with a thermal bath

at temperature T_i and described by the Langevin equation

$$\frac{dv_i}{dt} = -\frac{\alpha_i}{m}v_i + \bar{f}_i(t) + \xi_i(t), \quad (\text{A1})$$

where $\gamma_i = \alpha_i/m$. The above equation is formally identical to the overdamped harmonic oscillator subject to the force $f_i^*(x) = -\kappa x_i/m$, simply by replacing $x \rightarrow v$, $\kappa/\alpha \rightarrow \gamma_i$, and $1/\alpha \rightarrow \gamma_i/m$. Expressions for work, heat, and entropy production are obtained in the same way as in the underdamped case, by using the associated Fokker-Planck (FP) equation. In this case, the time evolution of the probability distribution $P_i(v, t)$ is given by

$$\frac{\partial P_i}{\partial t} = -\frac{\partial J_i}{\partial v} - \bar{f}_i(t) \frac{\partial P_i}{\partial v}, \quad (\text{A2})$$

where J_i denotes the probability current given by

$$J_i = -\gamma_i v P_i - \frac{\gamma_i k_B T_i}{m} \frac{\partial P_i}{\partial v}, \quad (\text{A3})$$

which is identical to Eq. (3). Applying the usual boundary conditions, in which both $P_i(v, t)$ and $J_i(v, t)$ vanish as $|v| \rightarrow \infty$, the time evolution of the system's energy $U_i(t) = m\langle v_i^2 \rangle/2$ allows us to obtain the main expressions for the thermodynamic quantities, identical to those presented in the main text [see, e.g., Eqs. (4)–(9)]. By averaging $\dot{W}_i(t)$ over a complete cycle, we also obtain relations identical to Eqs. (15) and (16), whose Onsager coefficients read as in [7,8]:

$$L_{11} = 1 - \frac{2}{\gamma\tau} \tanh\left(\frac{\gamma\tau}{4}\right) \quad (\text{A4})$$

and

$$L_{12} = \frac{2}{\gamma\tau} \tanh\left(\frac{\gamma\tau}{4}\right), \quad (\text{A5})$$

for constant drivings, where $L_{11} = L_{22}$ and $L_{12} = L_{21}$, and

$$L_{11} = \frac{1}{12\gamma\tau} \left\{ \gamma^3 \tau^3 - 3(\gamma^2 \tau^2 - 8) \coth\left(\frac{\gamma\tau}{2}\right) - 24 \text{csch}\left(\frac{\gamma\tau}{2}\right) \right\} \quad (\text{A6})$$

and

$$L_{12} = \frac{(-\gamma\tau + 2e^{\frac{\gamma\tau}{2}} - 2)(e^{\frac{\gamma\tau}{2}}(\gamma\tau - 2) + 2)}{2\gamma\tau(e^{\gamma\tau} - 1)} \quad (\text{A7})$$

for the linear drivings, respectively, where $L_{22} = L_{11}$ and $L_{12} = L_{21}$.

As a last comment, it is worth mentioning that a smooth crossover from the underdamped to the overdamped regime takes place by increasing γ . By taking the limit $\gamma \rightarrow \infty$ in the expression for $\langle v \rangle(t)$ given by Eq. (14), Fourier components match those for the overdamped case.

APPENDIX B: GENERAL FOURIER COEFFICIENTS OF THE MEAN VELOCITY AND GENERAL ONSAGER COEFFICIENTS

For the underdamped case, Fourier coefficients for the mean velocity, obtained via the solution of the system

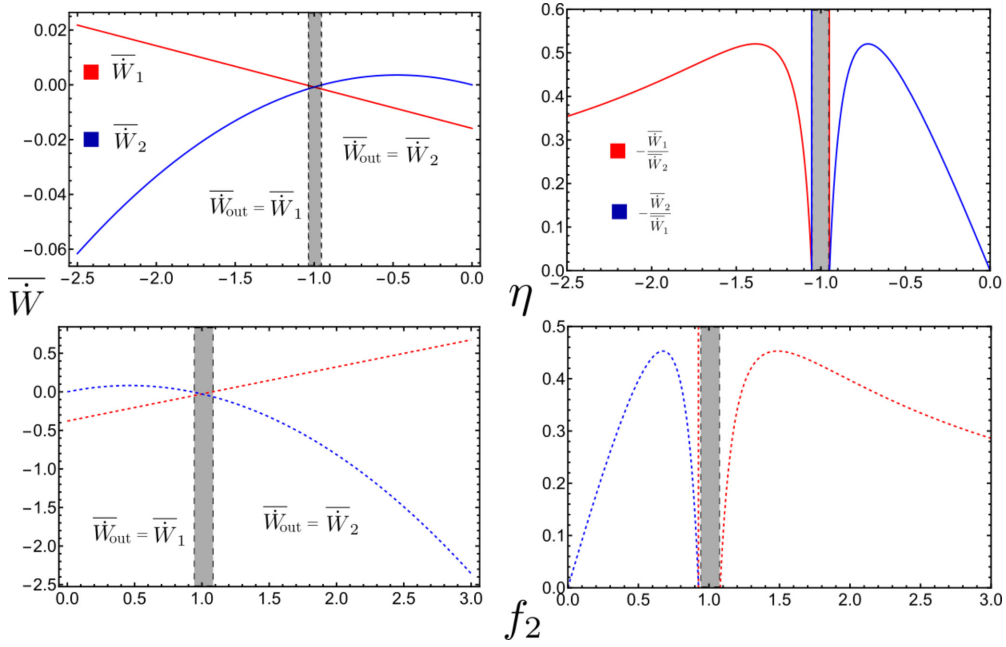


FIG. 6. Depiction of average powers \bar{W}_1 , \bar{W}_2 (left) and efficiencies (right) for the overdamped (top continuous lines) and for the underdamped (bottom dashed lines) for $f_1 = 1$. For better visualization, we adopted $\tau = 1$ in the overdamped case and $\tau = 5$ for the underdamped case. The dashed black lines represent the points where the exchange of fluxes $\bar{W}_{out} \leftrightarrow \bar{W}_{in}$ occurs and the gray region represents a “dud” regime.

equations, are listed below:

$$a_{1kv} = \frac{8\pi k \tau (8\pi \gamma k \tau a_n + b_n (\tau^2 (\gamma^2 - \omega_D^2) - 16\pi^2 k^2))}{(\tau^2 (\gamma - \omega_D)^2 + 16\pi^2 k^2)(\tau^2 (\gamma + \omega_D)^2 + 16\pi^2 k^2)},$$

$$a_{2kv} = \frac{8\pi k \tau (8\pi \gamma k \tau c_n + d_n (\tau^2 (\gamma^2 - \omega_D^2) - 16\pi^2 k^2))}{(\tau^2 (\gamma - \omega_D)^2 + 16\pi^2 k^2)(\tau^2 (\gamma + \omega_D)^2 + 16\pi^2 k^2)},$$

$$b_{1kv} = \frac{8\pi k \tau (a_n (\tau^2 (\omega_D^2 - \gamma^2) + 16\pi^2 k^2) + 8\pi \gamma k \tau b_n)}{(\tau^2 (\gamma - \omega_D)^2 + 16\pi^2 k^2)(\tau^2 (\gamma + \omega_D)^2 + 16\pi^2 k^2)},$$

and

$$b_{2kv} = \frac{8\pi k \tau (c_n (\tau^2 (\omega_D^2 - \gamma^2) + 16\pi^2 k^2) + 8\pi \gamma k \tau d_n)}{(\tau^2 (\gamma - \omega_D)^2 + 16\pi^2 k^2)(\tau^2 (\gamma + \omega_D)^2 + 16\pi^2 k^2)},$$

expressed in terms of Fourier coefficients a_n , b_n , c_n , and d_n for $g_1(t)$ and $g_2(t)$, respectively, and $\omega_D = \sqrt{\gamma^2 - 4\kappa}$ is the damped oscillation frequency of the system. Onsager coefficients are related to coefficients a_{ikv} and b_{ikv} via the following expressions:

$$L_{11} = T \sum_{n=1}^{\infty} \sum_{k=1}^{\infty} \frac{(\pi k a_{1kv} a_k - b_{1kv} (a_0 ((-1)^k - 1) - \pi k b_k))}{4\pi k} + (1 - \delta_{n,k}) \cdot \left(-\frac{((-1)^{k+n} - 1)(k a_n b_{1kv} - n a_{1kv} b_n)}{2\pi(k^2 - n^2)} \right),$$

$$L_{12} = T \sum_{n=1}^{\infty} \sum_{k=1}^{\infty} \frac{(\pi k a_{2kv} a_k - b_{2kv} (a_0 ((-1)^k - 1) - \pi k b_k))}{4\pi k} + (1 - \delta_{n,k}) \cdot \left(-\frac{((-1)^{k+n} - 1)(k a_n b_{2kv} - n a_{2kv} b_n)}{2\pi(k^2 - n^2)} \right),$$

$$L_{21} = T \sum_{n=1}^{\infty} \sum_{k=1}^{\infty} \frac{1}{4} \left(a_{1kv} c_k + \frac{c_0 ((-1)^k - 1) b_{1kv}}{\pi k} + b_{1kv} d_k \right) + (1 - \delta_{n,k}) \cdot \left(\frac{((-1)^{k+n} - 1)(k b_{1kv} c_n - n a_{1kv} d_n)}{2\pi(k^2 - n^2)} \right),$$

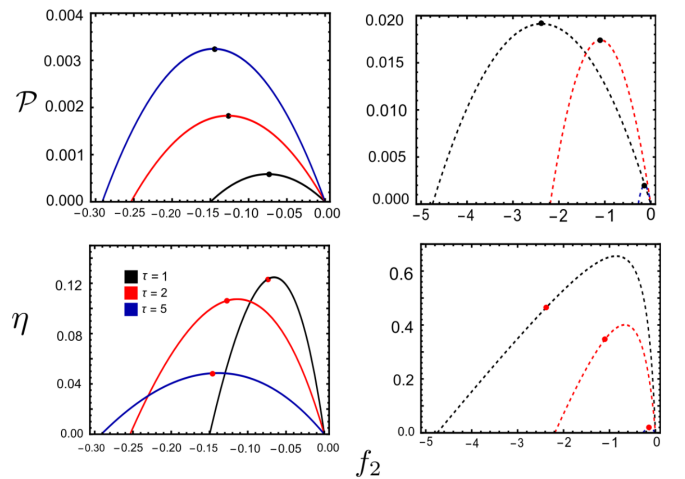


FIG. 7. Power output (top) and efficiency (bottom) versus f_2 for sinusoidal protocols and different periods τ . Dashed lines represent the underdamped regime, while continuous lines represent the overdamped regime. Black bullets are \mathcal{P}_{MP} and red bullets are η_{MP} . Parameters: $f_1 = 1$, $\gamma = 1$, and $\kappa = 1$.

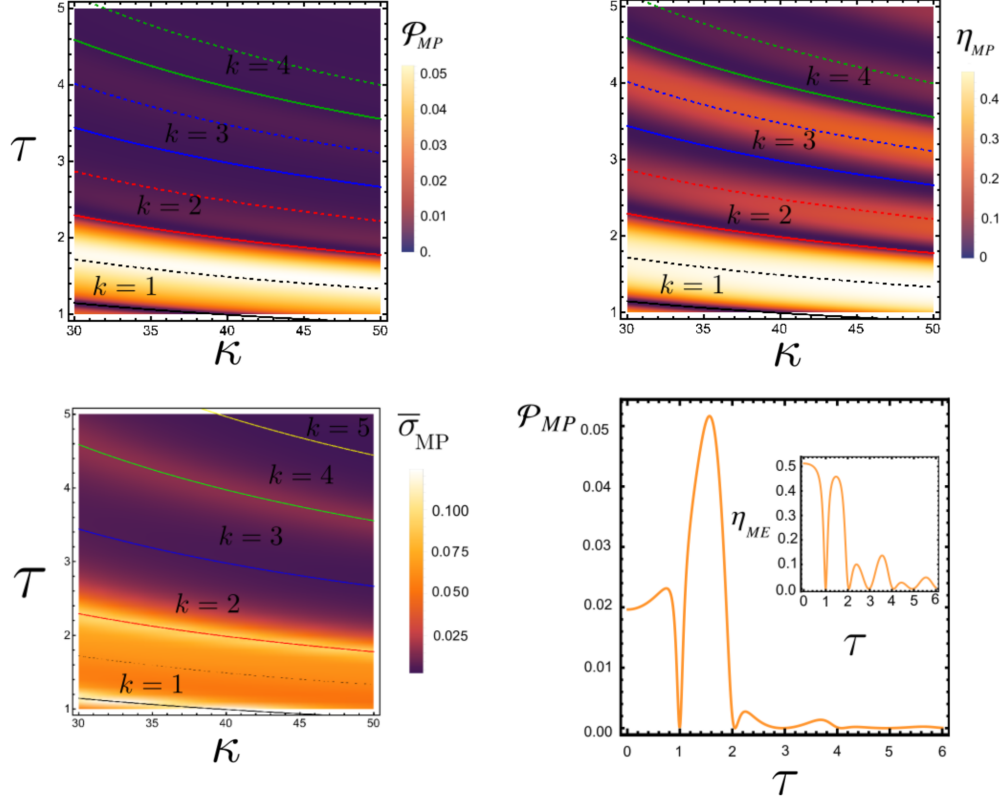


FIG. 8. Depiction of \mathcal{P}_{MP} , η_{MP} , and $\bar{\sigma}_{MP}$ heat maps for harmonic drivings. Right bottom panels show \mathcal{P}_{MP} and η_{ME} (inset) for $\kappa = 4\pi^2$. Parameters: f_1 and $\gamma = 1 = T = 1$.

and

$$L_{22} = T \sum_{n=1}^{\infty} \sum_{k=1}^{\infty} \frac{1}{4} \left(a_{2kv} c_k + \frac{c_0 ((-1)^k - 1) b_{2kv}}{\pi k} + b_{2kv} d_k \right) + (1 - \delta_{n,k}) \cdot \left(\frac{((-1)^{k+n} - 1) (k b_{2kv} c_n - n a_{2kv} d_n)}{2\pi (k^2 - n^2)} \right).$$

For constant and linear drivings, coefficients a_n , b_n , c_n , and d'_n s are listed below:

$$a_0 = c_0 = 1, \quad a_n = c_n = 0, \quad b_n = -d_n = \frac{-1 + (-1)^n}{\pi n} \quad (\text{B1})$$

for constant drivings and

$$a_0 = c_0 = \tau/4, \quad a_n = -c_n = \frac{((-1)^n - 1)\tau}{2\pi^2 n^2}, \quad d_n = -\frac{\tau}{2\pi n}, \quad (\text{B2})$$

and $b_n = (-1)^n d_n$ for linear drivings, respectively. For harmonic drivings, Fourier coefficients read $a_1 = d_1 = 1/2$, $a_n = d_n = 0 \forall n \neq 1$, $b_1 = c_1 = 0$, $b_n = (1 + (-1)^n)n/((n^2 - 1)\pi) = n \cdot c_n \forall n \neq 1$, and $c_0 = -2/\pi$. By inserting them into expressions for a_{1kv} , a_{2kv} , b_{1kv} , and b_{2kv} , Onsager coefficients can be promptly evaluated.

APPENDIX C: DISTINCT ENGINE OPERATION REGIMES

As discussed before in the main text, the interplay among parameters can generate two worksources with opposite sig-

nals, $\bar{W}_{in} < 0$ and $\bar{W}_{out} > 0$, representing the conversion of one form of energy (per time) into another one, the latter being identified as the power output. However, an interesting feature in both overdamped and underdamped cases relies on the fact that increasing the driving strength f_2 while keeping f_1 fixed (and analogously for the reverse situation) can change the regime operation. This is depicted in Fig. 6 by plotting $\bar{W}_1 \leftrightarrow \bar{W}_2$ as f_2 is changed. From Eqs. (5) and (15) and equal $L_{12} = L_{21}$ (the all cases here), we see that the change of regime occurs at $f_2^* = \pm \sqrt{L_{11}/L_{22}} f_1$. The efficiency is given by $\eta = -\bar{W}_1/\bar{W}_2$ for $f_2 < f_2^*$, and $1/\eta$ for $f_2 > f_2^*$, respectively. Since $L_{11} = L_{22}$ for constant and linear drivings and $f_1 = 1$, \bar{W}_1 presents a linear behavior, whether operating as \bar{W}_{in} or \bar{W}_{out} , whose regime crossover occurs at $f_2^* = -1$ and $f_2^* = 1$, for the overdamped and underdamped cases, respectively.

As a last comment, taking into account that the efficiency is given by the ratio between \bar{W}_{out} and \bar{W}_{in} , the crossover between regimes is characterized by infinitely large values of η (gray lines), in similarity with previous works [51].

APPENDIX D: SINUSOIDAL HARMONIC DRIVINGS

Sinusoidal driving forces appear in several contexts, such as for modeling Brownian particles under optical beam traps and optical tweezers [38–41], eletrophoresis process in colloidal gels [52], or even by measuring heat capacity experimentally by means of oscilating temperatures [53,54]. In this appendix we reproduce the aforementioned features for

harmonic drivings given by

$$\tilde{f}_i(t) = \begin{cases} X_1 \cos\left(\frac{2\pi}{\tau}t\right), & 0 \leq t \leq \tau/2 \\ X_2 \sin\left(\frac{2\pi}{\tau}t\right), & \tau/2 \leq t \leq \tau. \end{cases} \quad (\text{D1})$$

Figure 7 summarizes the main findings for the underdamped (right) and overdamped (left) panels. While \mathcal{P} increases as τ is increased (overdamped), the opposite trend is verified for the associated efficiencies and for the

underdamped case. In similarity with constant and linear drivings, the underdamped case not only presents substantial larger efficiencies and power outputs than the overdamped case but also it presents a remarkable larger operation regime.

Figure 8 depicts the resonant heat maps for sinusoidal drivings. They improves the power and efficiency, but they do not show remarkable improvements with respect to constant and linear drivings.

-
- [1] S. Carnot, *Réflexions Sur La Puissance Motrice Du Feu Sur Les Machinés Propre À Développer Cette Puissance*, édition critique par Fox Robert (Vrin J, Paris, 1978).
- [2] M. J. De Oliveira *et al.*, *Equilibrium Thermodynamics* (Springer, 2013).
- [3] U. Seifert, *Rep. Prog. Phys.* **75**, 126001 (2012).
- [4] C. Van den Broeck and M. Esposito, *Physica A* **418**, 6 (2015).
- [5] T. Tomé and M. J. de Oliveira, *Phys. Rev. E* **82**, 021120 (2010).
- [6] T. Tomé and M. J. de Oliveira, *J. Chem. Phys.* **148**, 224104 (2018).
- [7] A. L. L. Stable, C. E. F. Noa, W. G. C. Oropesa, and C. E. Fiore, *Phys. Rev. Res.* **2**, 043016 (2020).
- [8] C. E. F. Noa, A. L. L. Stable, W. G. C. Oropesa, A. Rosas, and C. E. Fiore, *Phys. Rev. Res.* **3**, 043152 (2021).
- [9] F. S. Filho, B. A. N. Akasaki, C. E. F. Noa, B. Cleuren, and C. E. Fiore, *Phys. Rev. E* **106**, 044134 (2022).
- [10] I. N. Mamede, A. L. L. Stable, and C. E. Fiore, *Phys. Rev. E* **106**, 064125 (2022).
- [11] K. Proesmans, Y. Dreher, M. Gavrilov, J. Bechhoefer, and C. Van den Broeck, *Phys. Rev. X* **6**, 041010 (2016).
- [12] K. Proesmans and C. Van den Broeck, *Chaos* **27**, 104601 (2017).
- [13] A. Rosas, C. Van den Broeck, and K. Lindenberg, *Phys. Rev. E* **96**, 052135 (2017).
- [14] J. M. Parrondo, J. M. Horowitz, and T. Sagawa, *Nat. Phys.* **11**, 131 (2015).
- [15] F. L. S. Rodrigues, G. De Chiara, M. Paternostro, and G. T. Landi, *Phys. Rev. Lett.* **123**, 140601 (2019).
- [16] P. Strasberg, G. Schaller, T. Brandes, and M. Esposito, *Phys. Rev. X* **7**, 021003 (2017).
- [17] O. A. D. Molitor and G. T. Landi, *Phys. Rev. A* **102**, 042217 (2020).
- [18] T. Sagawa, *J. Stat. Mech.: Theory Exp.* (2014) P03025.
- [19] K. Maruyama, F. Nori, and V. Vedral, *Rev. Mod. Phys.* **81**, 1 (2009).
- [20] C. H. Bennett, *Int. J. Theor. Phys.* **21**, 905 (1982).
- [21] P. E. Harunari, F. S. Filho, C. E. Fiore, and A. Rosas, *Phys. Rev. Res.* **3**, 023194 (2021).
- [22] N. G. Van Kampen, *Stochastic Processes in Physics and Chemistry* (Elsevier, 1954), Vol. 1.
- [23] T. Tomé and M. J. De Oliveira, *Stochastic Dynamics and Irreversibility* (Springer, 2015).
- [24] J. Tóthová and V. Lisý, *Eur. J. Phys.* **43**, 065103 (2022).
- [25] H. Safdari, A. G. Cherstvy, A. V. Chechkin, A. Bodrova, and R. Metzler, *Phys. Rev. E* **95**, 012120 (2017).
- [26] M. F. K. Pebeu, R. L. Woulaché, and T. C. Kofane, *Phys. Rev. E* **98**, 052107 (2018).
- [27] M. E. Fisher and A. B. Kolomeisky, *Proc. Natl. Acad. Sci. USA* **96**, 6597 (1999).
- [28] S. Leibler, *Nature (London)* **370**, 412 (1994).
- [29] A. S. Bodrova, A. V. Chechkin, A. G. Cherstvy, H. Safdari, I. M. Sokolov, and R. Metzler, *Sci. Rep.* **6**, 30520 (2016).
- [30] P. Nazé, S. Deffner, and M. V. Bonança, *J. Phys. Commun.* **6**, 083001 (2022).
- [31] S. De Karmakar and R. Ganesh, *Phys. Rev. E* **101**, 032121 (2020).
- [32] C. Van den Broeck and M. Esposito, *Phys. Rev. E* **82**, 011144 (2010).
- [33] D. M. Busiello and C. Fiore, *J. Phys. A: Math. Theor.* **55**, 485004 (2022).
- [34] S. Liepelt and R. Lipowsky, *Phys. Rev. Lett.* **98**, 258102 (2007).
- [35] S. Liepelt and R. Lipowsky, *Phys. Rev. E* **79**, 011917 (2009).
- [36] H. Hooyberghs, B. Cleuren, A. Salazar, J. O. Indekeu, and C. Van den Broeck, *J. Chem. Phys.* **139**, 134111 (2013).
- [37] Y. Luo, C. Zeng, and B. Li, *Europhys. Lett.* **137**, 21002 (2022).
- [38] B. Suassuna, B. Melo, and T. Guerreiro, *Phys. Rev. A* **103**, 013110 (2021).
- [39] L. P. Ghislain, N. A. Switz, and W. W. Webb, *Rev. Sci. Instrum.* **65**, 2762 (1994).
- [40] T. Davis, *Opt. Express* **15**, 2702 (2007).
- [41] M. J. Padgett, J. Molloy, and D. McGloin, *Optical Tweezers Methods and Applications* (CRC Press, 2010).
- [42] A. C. Barato and U. Seifert, *Phys. Rev. Lett.* **114**, 158101 (2015).
- [43] S. Otsubo, S. Ito, A. Dechant, and T. Sagawa, *Phys. Rev. E* **101**, 062106 (2020).
- [44] Y. Hasegawa and T. Van Vu, *Phys. Rev. E* **99**, 062126 (2019).
- [45] K. Proesmans and C. Van den Broeck, *Europhys. Lett.* **119**, 20001 (2017).
- [46] K. Proesmans, B. Cleuren, and C. Van den Broeck, *Phys. Rev. Lett.* **116**, 220601 (2016).
- [47] I. N. Mamede, P. E. Harunari, B. A. N. Akasaki, K. Proesmans, and C. E. Fiore, *Phys. Rev. E* **105**, 024106 (2022).
- [48] C. E. F. Noa, P. E. Harunari, M. J. de Oliveira, and C. E. Fiore, *Phys. Rev. E* **100**, 012104 (2019).
- [49] M. Aguilera, M. Igarashi, and H. Shimazaki, *Nat. Commun.* **14**, 3685 (2023).
- [50] S. A. M. Loos, S. H. L. Klapp, and T. Martynek, *Phys. Rev. Lett.* **130**, 198301 (2023).
- [51] F. S. Filho, G. A. L. Forão, D. M. Busiello, B. Cleuren, and C. E. Fiore, *Phys. Rev. Res.* **5**, 043067 (2023).
- [52] G. W. Slater, P. Mayer, and P. D. Grossman, *Electrophoresis* **16**, 75 (1995).
- [53] G. W. H. Höhne, W. Hemminger, and H.-J. Flammersheim, *Differential Scanning Calorimetry* (Springer, 2003), Vol. 2. pp. 147–244.
- [54] L. Filippov, *Int. J. Heat Mass Transf.* **9**, 681 (1966).